Non-Fermi Liquid at (2 + 1)D Ferromagnetic Quantum Critical Point

Xiao Yan Xu,[1] Kai Sun,[2] Yoni Schattner,[3] Erez Berg,[3] and Zi Yang Meng[1]

[1]*Beijing National Laboratory for Condensed Matter Physics and Institute of Physics, Chinese Academy of Sciences, Beijing 100190, China*

[2]*Department of Physics, University of Michigan, Ann Arbor, Michigan 48109, USA*

[3]*Department of Condensed Matter Physics, Weizmann Institute of Science, Rehovot, Israel 76100*

(Received 30 December 2016; revised manuscript received 17 July 2017; published 27 September 2017)

We construct a two-dimensional lattice model of fermions coupled to Ising ferromagnetic critical fluctuations. Using extensive sign-problem-free quantum Monte Carlo simulations, we show that the model realizes a continuous itinerant quantum phase transition. In comparison with other similar itinerant quantum critical points (QCPs), our QCP shows a much weaker superconductivity tendency with no superconducting state down to the lowest temperature investigated, hence making the system a good platform for the exploration of quantum critical fluctuations. Remarkably, clear signatures of non-Fermi liquid behavior in the fermion propagators are observed at the QCP. The critical fluctuations at the QCP partially resemble Hertz-Millis-Moriya behavior. However, careful scaling analysis reveals that the QCP belongs to a different universality class, deviating from both $(2+1)$D Ising and Hertz-Millis-Moriya predictions.

DOI: 10.1103/PhysRevX.7.031058

Subject Areas: Condensed Matter Physics, Strongly Correlated Materials

I. INTRODUCTION

Understanding the behavior of gapless fermionic liquids in the vicinity of a quantum phase transition is at the heart of strongly correlated electron systems, dating back to the celebrated Hertz-Millis-Moriya framework [1–3]. In particular, the question of Fermi-liquid instabilities at a magnetic (quantum) phase transition [4–9] and its applications to heavy-fermion materials [10,11] and transition-metal alloys (such as cuprates and pnictides [12,13]) is of vital importance and of broad interest to the condensed matter and high-energy physics communities.

On the other hand, to be able to obtain the understanding of quantum critical phenomena in itinerant electron systems is extremely challenging. Recently, extensive research efforts have been devoted to this question, utilizing advanced renormalization group analysis, including the two-dimensional (2D) Fermi surface coupled to a $U(1)$ gauge field, to Ising-nematic, or to spin-density-wave bosonic fluctuations [14–22]. Other approaches include dimensional regularization [23,24] and working in the limit of a large number of boson flavors [25]. Although important insights have been revealed from these studies, many fundamental questions still remain open. For example, will anomalous dimensions arise at such an itinerant quantum critical point (QCP)? The Hertz-Millis-Moriya theory predicts mean-field scalings. However, utilizing the effective field theory derived in Ref. [17], it was shown that divergence at four-loop order can lead to anomalous dimensions deviating from mean-field exponents [21]. In addition, the stability of these quantum critical points is also an open questions; e.g., will nonanalyticities in the momentum and frequency dependence of the theory lead to an instability towards a fluctuation-induced first-order transition or a fluctuation-induced second-order transition [26,27]? Moreover, various studies have suggested that near such a quantum critical point, critical fluctuations may trigger some other instability, resulting in a new phase that covers the QCP and masks the quantum critical region [28]. Experimentally, a ferromagnetic QCP was reported in a heavy-fermion metal [11].

Since analytical approaches are facing difficulties studying itinerant QCPs in a controlled manner, here, we study such a QCP by utilizing unbiased numerical calculations, i.e., the determinant quantum Monte Carlo (QMC) technique, which has been demonstrated as a very effective tool for such problems [29–37]. For the numerical studies on QCPs in itinerant fermionic systems, one major challenge lies in the fact that critical quantum fluctuations often trigger strong effective attractions between fermions, resulting in instabilities in the particle-particle channel. For example, in the recent studies on Ising nematic and charge-density-wave (CDW) QCPs, superconducting domes are observed covering the QCPs [29–33,35]. Although it is a very intriguing phenomenon that a QCP can induce unconventional superconductivity, for the study of quantum criticality itself, the induced superconducting dome makes it difficult to obtain direct information about the critical point for the following

two reasons. (1) To accurately measure the critical exponents, it is important to examine the close vicinity of the QCP, which becomes challenging if the QCP is buried inside a new quantum phase. (2) It is known that quantum criticality is one source for non-Fermi liquid behaviors. In order to understand and characterize such a non-Fermi liquid induced by a QCP, it is important to suppress other ordering in the quantum critical region. As a result, obtaining a pristine QCP without other induced instabilities becomes crucial for studying these QCPs, which is one main objective of this paper.

In this paper, we construct a model of 2D fermions interacting with gapless ferromagnetic (Ising) fluctuations and use the determinant QMC technique to solve this $(2+1)$D problem exactly [29–37]. Our QMC results are consistent with such a pristine continuous quantum phase transition in an itinerant ferromagnet in $(2+1)$D, with no superconducting ordering at any coupling strengths and down to the lowest temperature that we can access. The absence of superconductivity allows us to study the close vicinity of the QCP, where we found clear signatures of non-Fermi liquid behavior in the fermion propagators, induced by critical fluctuations. Furthermore, we find that because of the coupling between fermions and bosonic modes, the ferromagnetic QCP is different from an ordinary $(2+1)$D Ising transition [38], but it also deviates from the predictions of the Hertz-Millis-Moriya theory [6]. Hence, our results support the existence of a ferromagnetic QCP with markedly non-Fermi liquid behavior. These results broaden the theoretical understanding of itinerant quantum criticality and make connections to the existing experiment phenomena.

II. MODEL AND METHOD

We consider a two-dimensional lattice model of itinerant fermions coupled to an Ising ferromagnet with a transverse field [Fig. 1(a)]. The Hamiltonian is comprised of three parts,

$$\hat{H} = \hat{H}_f + \hat{H}_s + \hat{H}_{sf}, \tag{1}$$

$$\hat{H}_f = -t\sum_{\langle ij\rangle\lambda\sigma} \hat{c}^{\dagger}_{i\lambda\sigma}\hat{c}_{j\lambda\sigma} + \text{H.c.}, \tag{2}$$

$$\hat{H}_s = -J\sum_{\langle ij\rangle} \hat{s}^z_i\hat{s}^z_j - h\sum_i \hat{s}^x_i, \tag{3}$$

$$\hat{H}_{sf} = -\xi\sum_i s^z_i(\hat{\sigma}^z_{i1} + \hat{\sigma}^z_{i2}). \tag{4}$$

The fermionic part $\hat{H}_f$ describes spin-1/2 fermions on a square lattice with two independent orbitals per site ($\lambda = 1, 2$). It includes a nearest-neighbor hopping term that preserves the spin and orbital symmetries, where i and j label the sites, while σ and λ are the spin and orbital indices, respectively. We work in the grand canonical ensemble, where the fermion density is set by the chemical potential μ. All energy scales are measured in units of t. In addition, each site of the square lattice has an Ising spin $\hat{s}^z_i = \pm 1$, whose quantum dynamics are governed by a ferromagnetic transverse-field Ising model $\hat{H}_s$. The Ising spins and the fermions are coupled via an on-site Ising term $\hat{H}_{sf}$, where $\hat{\sigma}^z_{i\lambda} = (\hat{n}_{i\lambda\uparrow} - \hat{n}_{i\lambda\downarrow})/2$ is the z component of the fermion spin at orbit λ on site i.

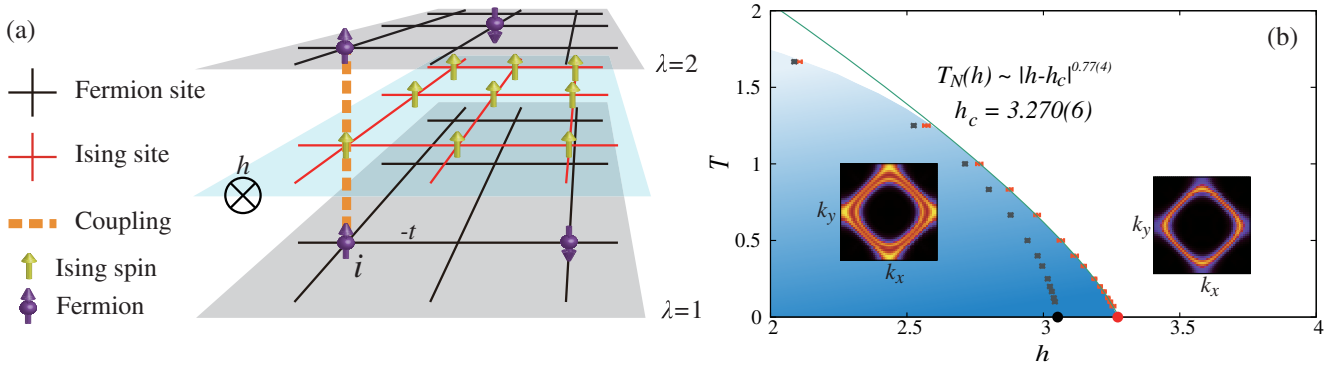

FIG. 1. (a) Sketches of our model shown in Eq. (1). Two bands or orbits ($\lambda = 1, 2$) of fermions move in a square lattice; at each site, the fermion spin is coupled to an Ising-gauge variable on the same lattice; and the Ising spins are subject to a ferromagnetic interaction J among themselves and a transverse magnetic field h. The quantum fluctuations of the transverse-field Ising model furthermore introduce effective interactions among the fermions. (b) $h-T$ phase diagram of our model in Eq. (1). The phase boundaries (orange data points) for coupling $\xi = 1$ and $\mu = -0.5$ (fermion density $\langle n_{i\lambda}\rangle \approx 0.8$) are the thermal transition points $T_N(h)$ from the ferromagnetic phase (FM) to the paramagnetic phase (PM). The FM phase is further highlighted by the shaded blue area. For comparison, we also plot the phase boundary without coupling (grey data points), i.e., that of the $(2+1)$D transverse-field Ising model. The coupling changes the position of the QCP (black dot to red dot along the h axis) as well as the power law of the phase boundary, which is described by critical exponents ν and z [$T_N(h) \sim |h-h_c|^{z\nu}$] with $\nu z = 0.63$ for $(2+1)$D Ising at $\xi = 0$ and $T_N(h) \sim |h-h_c|^c$ with $c = 0.77(4)$ for FM QCP at $\xi = 1$. The insets are plots of the low-energy spectral weight, $G[\mathbf{k}, \tau = (\beta/2)]$, in the FM phase (left) and the PM phase (right), shown for $L = 24$. Here, results from several different sets of twisted boundary conditions are superimposed (see Appendix B).

While, generically, models describing ferromagnetic transitions in fermionic systems suffer from the sign problem, here, the absence of the sign problem is guaranteed by the introduction of the two orbitals $\lambda = 1$ and 2. The two-orbital model is invariant under the antiunitary symmetry $i\tau_y K$, where τ_y is a Pauli matrix in the orbital basis and K is the complex conjugation operator; thus, it is free of sign problems [39]. The details of the DQMC implementation are presented in Appendix A.

The Hamiltonian in Eq. (1) possesses an $SU(2) \times SU(2) \times U(1) \times U(1) \times Z_2$ symmetry, where the two $SU(2)$ symmetries are independent rotations in the orbital basis for spin up and spin down, the two $U(1)$ symmetries correspond to conservation of particle number with spin up and spin down, and the Z_2 symmetry interchanges spin up and spin down while flipping the Ising spins $s_z \to -s_z$.

As h and T are reduced, the system undergoes a PM-FM phase transition, spontaneously breaking the Z_2 symmetry. In the absence of coupling between the Ising spins and the fermions, the transition belongs to the Ising universality class [40]. However, in the presence of the coupling ξ between the Ising spins and the fermions, the system becomes strongly correlated near the ferromagnetic QCP. Here, we focus on the properties of this exotic itinerant paramagnetic-ferromagnetic transition.

III. PHASE DIAGRAM

For $\xi = 0$, the Ising spins are decoupled from the fermions, and the phase transition is governed by the transverse-field Ising model. The phase diagram is shown in Fig. 1(b), where the phase boundary is marked by grey data points. Our numerical studies confirm that the phase boundary ends at a QCP at $T = 0$ with $(2+1)$D Ising universality class [40]. Near the QCP, the transition temperature follows the scaling relation, $T_N(h) \sim |h - h_c|^{\nu z}$ with $h_c = 3.04(2)$ and $\nu z = 0.63$, consistent with the literature [34,38].

We now study the itinerant PM-FM transition by turning on the coupling between the fermions and the Ising spins. We begin by setting the coupling strength $\xi = 1$ and chemical potential $\mu = -0.5$, which gives rise to a fermion density $\langle n_{i\lambda} \rangle \approx 0.8$. As shown in Fig. 1(b), turning on the coupling shifts FM phase boundary (orange data points) to higher values of T and h. At this coupling strength, down to the lowest temperature that we have accessed, $\beta = 100$ $(T = 0.01)$, we observe no signature of any additional ordered phases near the QCP. We identify the finite-temperature ferromagnetic transition by a finite-size scaling analysis of spin susceptibilities, as explained in Appendix C. Extrapolation towards zero temperature indicates that the itinerant PM-FM quantum phase transition occurs at $h_c = 3.270(6)$ and is of second order, but the scaling behavior near the QCP deviates strongly from that of the $(2+1)$D Ising universality class. For example, as shown in Fig. 1(b), the transition temperature T_N scales as $T_N(h) \sim |h - h_c|^c$ with $h_c = 3.270(6)$ and $c = 0.77(4)$. Note that because of the itinerant nature of the QCP, the exponent c is no longer expected to obey the relation $c = z\nu$ [6].

Because of the nonzero coupling ξ, the Fermi surface structure changes across the FM transition. The fermionic low-energy spectral weight shown in the inset of Fig. 1(b), extracted from the imaginary time Green's function $G(\tau = \beta/2)$ [30,41], reveals the location of the Fermi surface. In the PM phase $(h > h_c)$, fermions with up and down spins share the same Fermi surface because of the spin degeneracy (Ising symmetry) of the Hamiltonian [right inset of Fig. 1(b)]. This degeneracy is lifted in the FM phase $(h < h_c)$ because of spontaneous symmetry breaking, and thus, the Fermi surface splits [left inset of Fig. 1(b)].

At the QCP, low-energy fermionic excitations near the Fermi surface become strongly coupled with the critical bosonic spin fluctuations, offering an ideal platform for investigating the itinerant FM QCP. Below, we demonstrate that this QCP is stable down to low-energy scales and, more interestingly, that it is characterized by a dramatic breakdown of Fermi-liquid behavior.

IV. NON-FERMI LIQUID BEHAVIOR

One of the key theoretical predictions for an itinerant QCP is that the critical bosonic fluctuations induce strong damping of the fermions, resulting in a non-Fermi liquid where the low-temperature fermionic quasiparticle weight vanishes at the Fermi surface [14,16–18,22–24,42]. Following Ref. [43], we measure the quasiparticle weight from the Matsubara-frequency self-energy

$$Z_{\mathbf{k}_F} \approx \frac{1}{1 - \frac{\mathrm{Im}\Sigma(\mathbf{k}_F, i\omega_0)}{\omega_0}}, \tag{5}$$

where Σ is obtained from our QMC simulations and $\mathbf{k}_F$ is the momentum at the Fermi surface (FS). In our finite-temperature simulations, the Matsubara frequencies take discrete values, $\omega_n = \pi(2n+1)T$. As an estimator for $Z_{\mathbf{k}_F}$, we use the first Matsubara frequency, $\omega_0 = \pi T$ in Eq. (5).

The results are shown in Fig. 2(a) for $h = h_c$ (squares) and $h > h_c$ (circles). Here, we plot the quasiparticle weight at two different momentum points on the Fermi surface, i.e., $\mathbf{k}_F$ along the k_x direction $(\theta = 0)$ and along the $k_x = k_y$ direction $(\theta = (\pi/4))$. In the paramagnetic phase $(h > h_c)$, $Z(T)$ remains close to unity at low temperatures, indicating well-defined quasiparticles on the Fermi surface, as expected in a Fermi liquid. In contrast, at the QCP $(h = h_c)$, $Z(T)$ is suppressed with decreasing temperature and it extrapolates to zero at $T \to 0$, which is the key signature of a non-Fermi liquid. This is one of the key findings of this study.

As shown in Fig. 2(a), at the QCP, as $T \to 0$, $Z(T)$ decreases faster for $\mathbf{k}_F$ along the diagonal direction

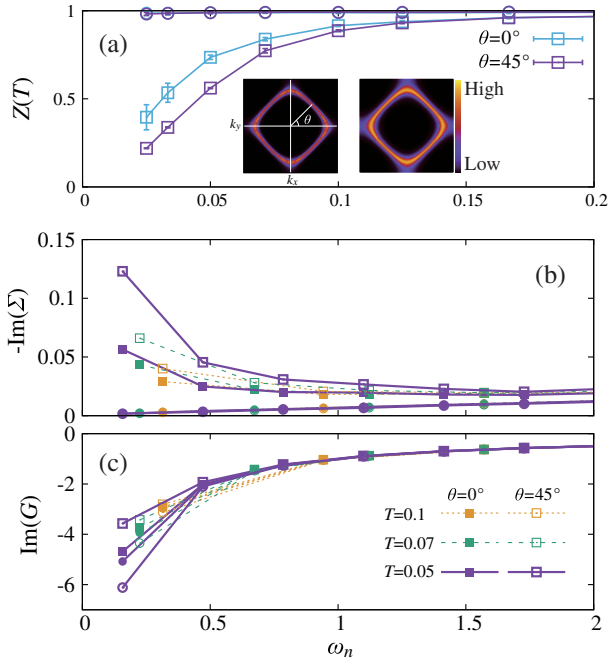

FIG. 2. (a) $Z_{\mathbf{k}_F}(T)$ at FM QCP ($h_c = 3.27$, squares) and in the PM phase ($h = 3.60$, circles). The left inset is the $G[\mathbf{k}, (\beta/2)]$ at the FS for $T = 0.05$, while the right inset is for $T = 0.1$. Although there is anisotropy in $Z_{\mathbf{k}_F}$ at different parts of the FS, the quasiparticle weight in the k_x and $k_x = k_y$ directions both approach zero at FM QCP, indicating a non-Fermi liquid behavior for the entire FS. The data in the PM phase show the quasiparticle weight approaching a constant (very close to 1), indicating the system is a Fermi liquid. Panel (b) shows $-\mathrm{Im}(\Sigma(\mathbf{k}_F, \omega_n))$ at FM QCP ($h = h_c$, square symbol). It increases as $\omega_n \to 0$ (signifying the system at QCP loses its quasiparticle weight with a power law), a non-Fermi liquid behavior, while in the PM phase ($h = 3.60$, circle symbol), the imaginary part of the self-energy approaches zero linearly as $\omega_n \to 0$—a Fermi-liquid behavior. (c) Imaginary part of the single-fermion Green's function at the FM QCP ($h = 3.27$, square symbol) and in the PM phase ($h = 3.60$, circle symbol). No signature of the gap formation is observed.

($\theta = (\pi/4)$) in comparison with other parts of the FS (e.g., $\theta = 0$). This anisotropy is due to the anisotropy of the Fermi surface. The fermion density in our simulation is around 0.8, which is not far from perfect nesting (at half-filling). This near-nesting Fermi-surface geometry results in soft fermion-bilinear modes around $\mathbf{Q} = (\pi, \pi)$, which we have directly observed by measuring the fermion spin susceptibility as shown in Appendix H. These soft modes have a finite gap, and thus they are not the origin of the non-Fermi liquid behavior. However, scattering with these soft modes presumably introduces additional dampings for the fermions. Such scattering processes are stronger (weaker) for $\mathbf{k}_F$ near the diagonal direction $\theta = (\pi/4)$ ($\theta = 0$), where $2\mathbf{k}_F$ is close to (far away from) $\mathbf{Q}$, and thus can lead to the observed anisotropy in $Z(T)$.

In Fig. 2(b), we show the imaginary part of the self-energy, $\Sigma(\omega_n) = G_0^{-1} - G^{-1}$ [where $G(\omega_n)$ and $G_0(\omega_n)$ are the fermionic Green's function, and the Green's function of the noninteracting system, respectively] as a function of the Matsubara frequency ω_n. In the paramagnetic phase (circle symbols), $-\mathrm{Im}(\Sigma)$ approaches zero linearly as $\omega_n \to 0$, as expected for a Fermi liquid. Such a behavior is not seen at the QCP, however, where we observe an *increase* of $-\mathrm{Im}(\Sigma)$ upon decreasing ω_n, indicating a strong damping of the fermions at low frequencies. One possible mechanism for such surprising frequency dependence is related to thermal fluctuations of the FM order parameter, as shown in Appendix I.

The fermion Green's functions, $\mathrm{Im}G(\mathbf{k}_F, \omega_n)$, are presented in Fig. 2(c). Note that $-\mathrm{Im}G(\mathbf{k}_F, \omega_n)$ is related to the single-fermion spectral function $A(\mathbf{k}_F, \omega)$ through $-\mathrm{Im}G(\omega_n) = \int[(d\omega)/\pi][\omega_n/(\omega_n^2 + \omega^2)]A(\mathbf{k}_F, \omega)$. The fact that $-\mathrm{Im}(G)$ increases with decreasing ω_n indicates that, both for $h = h_c$ and $h > h_c$ and to the lowest temperature we have accessed, there is no visible suppression of the fermionic spectral weight at low frequency, i.e., no sign of an opening of a gap in the fermionic spectrum (at least down to frequencies of the order of $\omega \sim \pi T$). A similar conclusion can be reached by noting that $-\mathrm{Im}\Sigma$ is never much larger than ω_0; i.e., the self-energy never dominates over the bare frequency dependence of the Green's function. This observation is consistent with the fact that there is no signature of a nearby superconducting phase for any value of h, as shown in Sec. VI and Appendix G. Similarly, there is no signature of any other competing phase that emerges close to the QCP (see Appendix H).

V. QUANTUM CRITICAL SCALING ANALYSIS

Near the quantum critical point, the bosonic critical modes become strongly renormalized by the coupling to the gapless fermionic degrees of freedom (d.o.f.). As a result, the universality class of the quantum critical point is different from that of an ordinary Ising transition in $(2 + 1)$ dimensions. Our QMC results indicate that the behavior at the QCP resembles the behavior predicted by Hertz-Millis theory but also deviates from it in a significant way. Below, we first summarize the Hertz-Millis predictions and then present a modified Hertz-Millis scaling formula, which fits our QMC data for the Ising spin susceptibility at all the momenta and frequencies simulated.

The Hertz-Millis-Moriya theory is based on quantum dynamics obtained from the random phase approximation (RPA) [1–3]. Within this approximation, the Ising spin susceptibility, $\chi(h, T, \mathbf{q}, \omega_n) = (1/L^2)\int d\tau \sum_{ij} e^{i\omega_n\tau - i\mathbf{q}r_{ij}}\langle s_i^z(\tau)s_j^z(0)\rangle$, takes the following form near the QCP,

$$\chi(h, T, \mathbf{q}, \omega_n) = \frac{1}{c_t T^2 + c_h|h - h_c| + c_q q^2 + c_\omega \omega^2 + \Delta(\mathbf{q}, \omega_n)}, \quad (6)$$

where c_t, c_h, c_q, c_ω are constants. Here, $c_q q^2 + c_\omega \omega^2$ comes from the bare action of the Ising d.o.f., and the $\Delta(\mathbf{q}, \omega_n)$ term is the contribution of the fermionic fluctuations. For an isotropic 2D Fermi fluid, and for q and ω_n much smaller than the Fermi momentum and energy, respectively,

$$\Delta(\mathbf{q}, \omega_n) = c_{\mathrm{HM}} \frac{|\omega_n|}{\sqrt{\omega_n^2 + (v_f q)^2}}, \tag{7}$$

where c_{HM} is a constant and v_f is the Fermi velocity. A key property of $\Delta(\mathbf{q}, \omega_n)$ is its singular behavior in the limit $q \to 0$, $\omega \to 0$. Depending on whether one first takes the long-wavelength ($q \to 0$) limit or the low-energy ($\omega \to 0$) limit, $\Delta(\mathbf{q}, \omega_n)$ converges to different values, $\lim_{q\to 0}\lim_{\omega_n \to 0}\Delta(\mathbf{q}, \omega_n) \sim \omega_n/q \to 0$, while $\lim_{\omega_n \to 0}\lim_{q\to 0}\Delta(\mathbf{q}, \omega_n) = c_{\mathrm{HM}}$. This singularity is of great importance for the quantum dynamics at the QCP. It leads to the following properties:

$$\chi(h = h_c, T = 0, \mathbf{q}, \omega_n = 0)^{-1} = c_q q^2, \tag{8}$$

$$\chi(h = h_c, T = 0, \mathbf{q} = 0, \omega_n)^{-1} = c_{\mathrm{HM}} + c_\omega \omega_n^2. \tag{9}$$

Beyond the RPA level, the scaling relation above can be modified by higher-order terms, and the scaling analysis in Ref. [2] suggests that the exponent for T shifts from 2 to 1 up to logarithmic corrections.

Although these two relations differ by a constant (c_{HM}), note that the q and ω_n dependence has the same scaling exponent. The reason for this behavior is that at $q = 0$ and small ω_n (or at $\omega_n = 0$ and small q), $\Delta(\mathbf{q}, \omega_n)$ becomes independent of q or ω_n, respectively. Thus, the ω_n or q dependence in χ^{-1} is dominated by the bare action of the Ising d.o.f. The fact that the exponents characterizing the ω and q dependence are the same reflects the emergent Lorentz symmetry of the bare Ising action.

Our QMC results share some characteristics with this predicted form but with anomalous scaling dimensions. As shown in Figs. 3(a) and 3(b), we indeed find that $\lim_{q\to 0}\lim_{\omega_n \to 0}\chi^{-1}(\mathbf{q}, \omega_n)$ differs from $\lim_{\omega_n \to 0}\lim_{q\to 0}\chi^{-1}(\mathbf{q}, \omega_n)$ by a constant $c_{\mathrm{HM}} = 0.20(4)$ as predicted by the RPA. The ferromagnetic susceptibility is found to be well described by the following formula:

$$\chi(h, T, \mathbf{q}, \omega_n) = \frac{1}{c_t T^{a_t} + c_h |h - h_c|^{\gamma} + (c_q q^2 + c_\omega \omega^2)^{a_q/2} + \Delta(\mathbf{q}, \omega_n)}, \tag{10}$$

with an anomalous exponent $a_q = 1.85(3)$. This is different both from the exponent for an Ising transition in $(2+1)$ dimensions, 1.96, and from the Hertz-Millis value of 2.

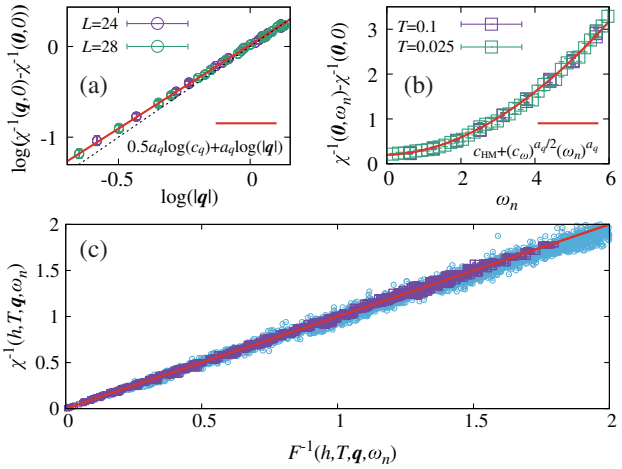

FIG. 3. (a) Inverse spin susceptibility at $\omega_n = 0$ as a function of $|\mathbf{q}|$ (data points with $L = 24$, 28 and $T = 0.125$). The red line shows the fitting with $\chi^{-1} = c_q q^{a_q}$, and we get $a_q = 1.85(3)$. The black dashed line shows the slope $a_q = 2$. (b) Inverse spin susceptibility at $q = 0$ as a function of ω_n (data points with $L = 20$, 24, and 28 for $T = 0.1$, with $L = 20$ for $T = 0.025$). The red curve shows the fitting with $\chi^{-1} = c_{\mathrm{HM}} + c_\omega \omega_n^{a_\omega}$. (c) Data collapse for Ising susceptibility against the functional Eq. (10), where $F^{-1} = c_t T^{a_t} + c_h |h - h_c|^{\gamma} + (c_q q^2 + c_\omega \omega^2)^{a_q/2} + \Delta(\mathbf{q}, \omega_n)$. The dark violet squares (3946 in total, made up of $T = 1.0$, 0.83, 0.67, 0.5, 0.4, 0.3, 0.25, 0.2, 0.17, 0.13, 0.1; $h = 3.27$,3.3,3.4,3.5,3.6,3.7,3.8,3.9,4.0; and $L = 24$) are for data with zero frequency, while the light blue circles (6096 in total, made up of $L = 20$ with $T = 0.1$, 0.05, 0.033, 0.025, 0.014, 0.01, and $L = 24$, 28 with $T = 0.1$, 0.05) are for data with frequency dependence. The red line with $y = x$ serves as the baseline for comparison of QMC data with the functional approximation.

The presence of an anomalous exponent is another key finding of this study.

The functional form in Eq. (10) is analogous to the RPA prediction [Eq. (6)], but it allows for non-mean-field exponents (a_t, γ, and a_q). This form is found to fit all the numerical data points [Fig. 3(c)].

Note that Eq. (10) contains $\Delta(\mathbf{q}, \omega_n)$, which has the form of a free-fermion susceptibility. However, as will be shown below, within numerical resolution, as long as Δ captures the singular behavior at $q \to 0$ and $\omega \to 0$, the quality of the fit of $\chi(h, T, \mathbf{q}, \omega_n)$ is not sensitive to the detailed functional form of $\Delta(\mathbf{q}, \omega_n)$. More importantly, our key conclusions, e.g., the anomalous dimension $\eta = 2 - a_q = 0.15$, are fully independent of the particular choice of $\Delta(\mathbf{q}, \omega_n)$. Therefore, here we use the RPA form [Eq. (7)], where, for simplicity, we set v_f to 2.

By fitting with $\chi(h, T)$ at $q = 0$ and $\omega_n = 0$, we find that $c_t = 0.13(1)$, $a_t = 1.48(4)$, $c_h = 0.7(1)$, $\gamma = 1.18(4)$; details can be found in Appendix D. As shown above, by fitting with χ at $q = 0$ or $\omega = 0$ [Figs. 3(a) and 3(b)], we find $a_q = 1.85(3)$, $c_q = 1.00(2)$, $c_\omega = 0.10(2)$, and $c_{\mathrm{HM}} = 0.20(4)$. With all the fitting parameters fixed, we can use Eq. (10) to collapse all χ data for all q, ω_n, h, and T.

The results are presented in Fig. 3(c). Clearly, all the data collapse onto the same curve, especially at small q, ω_n, low temperature T, and $h \sim h_c$.

For $\Delta(\mathbf{q},\omega_n)$, we find that as long as $\lim_{\omega_n\to 0}\Delta(\mathbf{q},\omega_n)=0$ and $\lim_{q\to 0}\Delta(\mathbf{q},\omega_n) = c_{\mathrm{HM}} = 0.20(4)$, modifying the functional form of $\Delta(\mathbf{q},\omega_n)$ has little impact on χ within numerical error bars of the QMC data. This uncertainty in $\Delta(\mathbf{q},\omega_n)$ prevents us from obtaining detailed information about the dynamics at the QCP (e.g., the precise value of the dynamical critical exponent z). However, since by definition $\Delta(\mathbf{q},\omega_n)$ vanishes at $\omega_n = 0$, all the conclusions regarding the static limit ($\omega_n = 0$), including the anomalous dimensions $\eta = 2 - a_q = 0.15$ obtained from the q dependence in $\chi(\mathbf{q},\omega_n = 0)$, are independent of the details of $\Delta(\mathbf{q},\omega_n)$.

VI. SUPERCONDUCTIVITY

We now discuss the superconducting properties close to the FM QCP. Unlike previous QMC studies of quantum criticality in metals (such as the Ising-nematic, SDW, and other QCPs [29–33,35]), the FM QCP shows a substantial separation of scales between the onset of superconducting correlations and the phenomena described thus far, i.e., non-Fermi liquid behavior and quantum critical scaling, thus making this system an ideal platform for the investigation of quantum fluctuations close to criticality.

As described in Appendix E, the spin fluctuations induce an attractive interaction in the spin-triplet channel. The two-band structure of the model allows for a number of distinct superconducting order parameters, of which we find that the strongest pairing tendencies occur in the orbital-singlet, spin-triplet channel, with the order parameter

$$\Delta_{i,\sigma} = c_{i1\sigma}c_{i2\sigma}, \tag{11}$$

where $\sigma = \uparrow, \downarrow$ is the spin index. Indeed, this channel is found to be the leading instability in a weak-coupling, mean-field analysis (see Appendix E). The two components $\Delta_\uparrow$ and $\Delta_\downarrow$ are related by the Z_2 (spin-flip) symmetry of the model and are therefore of equal magnitude in the magnetically disordered phase. The order parameter transforms as a scalar under lattice rotations and reflections; hence, we expect single-fermion excitations to be fully gapped in the superconducting state.

Because fermions in our model only preserve a $U(1)$ spin rotational symmetry, a finite-temperature triplet ordering is, in principle, allowed, in contrast to 2D systems with $SU(2)$ spin rotational symmetry where triplet pairing may only occur at zero temperature. As shown in Appendix F, the two-component nature of the order parameter allows, in principle, for more exotic phases such as a charge-4e superconductor (4e SC) and a spin-nematic (SN) phase [44–47]. We have found no numerical evidence for the existence of these phases, and therefore, we focus on the triplet, charge $2e$ superconductor described above.

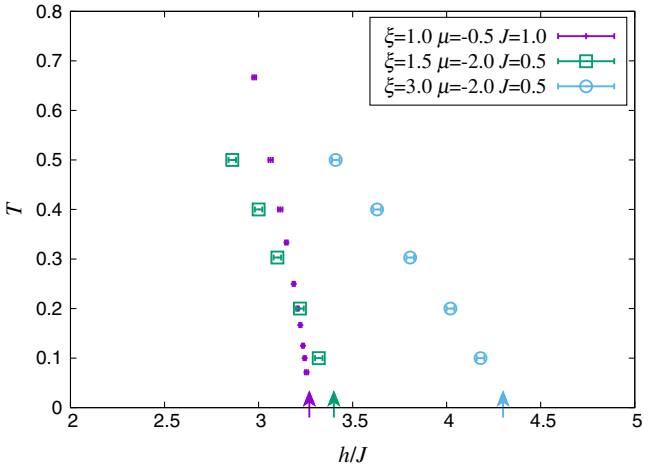

FIG. 4. Estimation of the FM QCP for larger coupling. There are three parameter sets in total: $\{\xi = 1.0, \mu = -0.5, J = 1.0\}$, $\{\xi = 1.5, \mu = -2, J = 0.5\}$, and $\{\xi = 3.0, \mu = -2, J = 0.5\}$. The finite-temperature phase boundaries are determined from the Ising spin susceptibilities, as discussed in Appendix D. The QCPs are denoted by the colored arrows. Close to each FM QCP, we scan h to measure various superconductivity instabilities. The results are shown in Fig. 5.

To probe for superconducting tendencies near the QCP, we explore three parameter sets: $\{\xi = 1.0, \mu = -0.5, J = 1.0\}$, $\{\xi = 1.5, \mu = -2, J = 0.5\}$, and $\{\xi = 3.0, \mu = -2, J = 0.5\}$. First, the finite-temperature FM-to-PM phase transitions are identified by finite-size scaling of the Ising spin susceptibilities, as discussed in Appendix D. Then, as depicted in Fig. 4, the FM QCPs are located by extrapolating the finite-temperature phase boundary towards $T = 0$. As expected, the larger the coupling ξ, the higher the critical field h_c at the FM QCP.

Next, we calculate the pairing correlations for all pairing channels, with on-site and nearest-neighbor form factors (see Appendix G). Among all the available channels, only the order parameter defined in Eq. (11) has pairing correlations peaked at the QCP. We conclude that it is the only channel that is substantially enhanced by critical FM fluctuations.

Figure 5 shows the pairing structure factor $C = [1/(2L^2)]\sum_{ij\sigma}\langle\Delta^\dagger_{i\sigma}\Delta_{j\sigma}\rangle$. At all couplings, we find a peak of the pairing correlations at the QCP. At $\xi = 1$ and $\xi = 1.5$, the pairing correlations do not grow with the system size, indicating we are far from a superconducting transition. At the strongest coupling, $\xi = 3$, C grows, albeit very slowly, with L, indicating that the correlation length of the superconducting order parameter is moderately large.

Although pairing correlations in this channel are enhanced close to the QCP, long-range or quasi-long-range superconducting order never develops down to $T = 0.025$ for any of the three parameter sets. This conclusion is corroborated by an analysis of the superfluid density, shown in Appendix G.

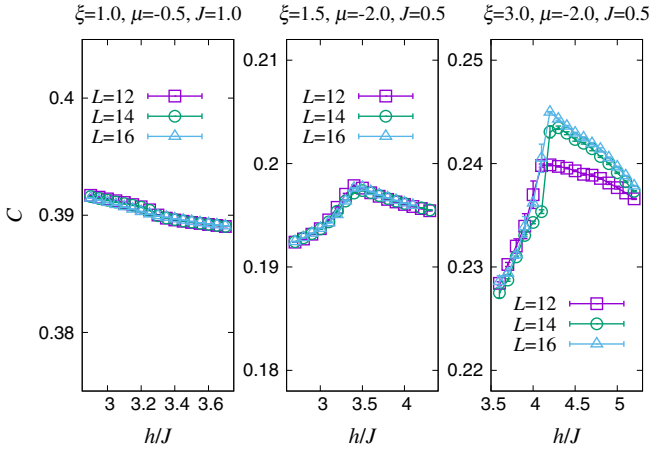

FIG. 5. Static pairing-correlation function $C = (1/L^2)\langle\hat{\Delta}^\dagger\hat{\Delta}\rangle$ for order parameters defined in Eq. (11). For $\{\xi = 1.0, \mu = -0.5, J = 1.0\}$, no enhancement of pairing correlation functions is observed in any pairing channel down to $T = 0.025$. For $\{\xi = 1.5, \mu = -2, J = 0.5\}$ and $\{\xi = 3.0, \mu = -2, J = 0.5\}$, the pairing order parameters $\Delta_\uparrow$ and $\Delta_\downarrow$ show enhanced correlation near the QCP, in agreement with theoretical analysis. No enhancement is observed in other pairing channels.

VII. DISCUSSION

In this work, we have constructed a lattice model that realizes a pristine ferromagnetic QCP in an itinerant Fermi system. At the QCP, clear non-Fermi liquid behavior is observed. The static ($\omega_n = 0$) ferromagnetic susceptibility obeys scaling with an anomalous dimension $\eta = 2 - a_q = 0.15$, which deviates from both the $(2+1)$D Ising value ($\eta = 0.036$) and the mean-field value expected from Hertz-Millis theory ($\eta = 0$).

The ω_n dependence of the bosonic susceptibility is highly nontrivial. In particular, the long-wavelength limit ($q \to 0$) and the low-frequency limit ($\omega_n \to 0$) do not commute. To fully characterize the quantum dynamics at the QCP, we need to obtain detailed information about $\Delta(\mathbf{q}, \omega_n)$ in Eq. (10), especially in the low-energy limit. The presence of an anomalous dimension in a_q and in transition temperature T_N suggests that Δ probably also deviates from the Hertz-Millis form, which has a dynamic critical exponent $z = 3$ and thus predicts mean-field exponents. At the qualitative level, our conclusions and the observation of anomalous dimensions are in good agreement with the four-loop scaling analysis in Ref. [21]. However, although our studies reveal direct information on the qualitative features of $\Delta(\mathbf{q}, \omega_n)$ (i.e., the singular behavior in the limit $q \to 0$, $\omega_n \to 0$), the detailed functional form is beyond the resolution set by finite-size and finite-temperature effects of our QMC study.

It is interesting to contrast the results of the present study with those obtained for a related (but different) problem of an itinerant Ising-nematic QCP [30,35]. The two problems have essentially the same description within Hertz-Millis theory. Similarly to our results for an Ising ferromagnetic QCP, the Ising nematic QCP displays strong deviations from Fermi-liquid behavior. A key difference, however, is that in the FM QCP, Fermi-liquid behavior is lost everywhere along the Fermi surface; i.e., there are no "cold spots" with long-lived quasiparticles. Furthermore, near the FM QCP, strong deviations from Fermi-liquid behavior were found at temperatures much larger than any scale associated with superconductivity. In the Ising-nematic problem, the Ising order parameter correlations also show a singular behavior in the $(q \to 0, \omega_n \to 0)$ limit. However, in the FM case presented here, the fermionic magnetic susceptibility is exactly conserved, unlike the Ising-nematic case where an approximate conservation was found. An additional key difference is the anomalous exponents detected in the present work.

Perhaps the most striking difference between the two models lies in their superconducting properties. While the Ising-nematic QCP was found to be strongly unstable towards s-wave superconductivity [35], the leading superconducting instability in the FM case is described by a two-component, spin-triplet order parameter, with the possibility of exhibiting interesting, unconventional phases such as a charge-4e superconductor.

On the experimental side, our results may shed some new light on the study about 2D or quasi-2D metallic materials with Ising magnetic order, like $Fe_{1/4}TaS_2$ [48] and $CeCd_3As_3$ [49].

ACKNOWLEDGMENTS

The authors thank F. Assaad and S. Kivelson for helpful discussions. X. Y. X. and Z. Y. M. are supported by the Ministry of Science and Technology of China under Grant No. 2016YFA0300502, the National Science Foundation of China under Grants No. 11421092 and No. 11574359, and the National Thousand-Young-Talents Program of China. We thank the following institutions for allocation of CPU time: the Center for Quantum Simulation Sciences in the Institute of Physics, Chinese Academy of Sciences; the Tianhe-1A platform at the National Supercomputer Center in Tianjin; and the Gauss Centre for Supercomputing e.V. [50] for providing access to the GCS Supercomputer SuperMUC at Leibniz Supercomputing Centre (LRZ, [51]). K. S. is supported by the National Science Foundation under Grants No. PHY-1402971 at the University of Michigan and the Alfred P. Sloan Foundation. Y. S. and E. B. were supported by the Israel Science Foundation under Grant No. 1291/12, by the US-Israel BSF under Grant No. 2014209, and by a Marie Curie reintegration grant. E. B. was supported by an Alon grant. Y. S. and E. B. thank S. Lederer and S. Kivelson for a collaboration on related topics.

APPENDIX A: DETERMINANTAL QUANTUM MONTE CARLO IMPLEMENTATIONS

The determinantal quantum Monte Carlo (DQMC) formalism starts with the partition function of the original Hamiltonian. To efficiently evaluate the trace in the partition function, discretized imaginary time is used and

$\beta = M\Delta\tau$ ($\Delta\tau = 0.05$). As the studied model contains both fermion and Ising d.o.f., the trace will involve both a sum over Ising spin configurations and a determinant after tracing out the fermion d.o.f.

$$Z = \mathrm{Tr}[e^{-\beta\hat{H}}] = \sum_{s_1^z\cdots s_N^z=\pm 1} \mathrm{Tr}_F\langle s_1^z\cdots s_N^z|(e^{-\Delta\tau\hat{H}})^M|s_1^z\cdots s_N^z\rangle. \quad \text{(A1)}$$

Let $\mathbf{S} = (s_1^z\cdots s_N^z)$ denote the Ising spins; then,

$$Z = \sum_{\mathbf{S}_1\cdots\mathbf{S}_M} \mathrm{Tr}_F\langle\mathbf{S_1}|e^{-\Delta\tau\hat{H}}|\mathbf{S}_M\rangle\langle\mathbf{S_M}|e^{-\Delta\tau\hat{H}}|\mathbf{S}_{M-1}\rangle \cdots\langle\mathbf{S_2}|e^{-\Delta\tau\hat{H}}|\mathbf{S}_1\rangle. \quad \text{(A2)}$$

Now we can trace out the fermion d.o.f. and obtain the configurational weight,

$$\omega_C = \omega_C^{TI}\omega_C^F \quad \text{(A3)}$$

with the Ising part

$$\omega_C^{TI} = \left(\prod_\tau\prod_{\langle i,j\rangle} e^{\Delta\tau J s_{i,\tau}^z s_{j,\tau}^z}\right)\left(\prod_i\prod_{\langle\tau,\tau'\rangle}\Lambda e^{\gamma s_{\tau,i}^z s_{\tau',i}^z}\right), \quad \text{(A4)}$$

where $\Lambda^2 = \sinh(\Delta\tau h)\cosh(\Delta\tau h)$, $\gamma = -\frac{1}{2}\ln(\tanh(\Delta\tau h))$. For the fermion part, we have

$$\omega_C^F = \det(\mathbf{1} + \mathbf{B}_M\cdots\mathbf{B}_1). \quad \text{(A5)}$$

As an antiunitary symmetry $i\tau_y K$ (where τ_y is a Pauli matrix in the orbital basis and K is the complex conjugation operator) makes the Hamiltonian invariant, the fermion part weight can be further rewritten as

$$\omega_C^F = \left|\prod_\sigma \det(\mathbf{1} + \mathbf{B}_M^{1\sigma}\cdots\mathbf{B}_1^{1\sigma})\right|^2, \quad \text{(A6)}$$

where

$$\mathbf{B}_\tau^{\lambda\sigma} = \exp(-\Delta\tau\mathbf{K}^{\lambda\sigma} + \Delta\tau\xi\,\mathrm{diag}(s_1^z,\ldots,s_N^z)), \quad \text{(A7)}$$

with $\mathbf{K}^{\lambda\sigma}$ the hopping matrix for orbital λ and spin σ. It turns out that both the fermion weight and the Ising weight are always positive; thus, there is no sign problem. To systematically improve the simulation, especially close to the (quantum) critical point, we have implemented both a local update in DQMC and a space-time global update [34]. In the global update, we use the Wolff algorithm [52] to propose space-time clusters of the Ising spins and then calculate the fermion weight to respect the detailed balance as the acceptance rate of the update. Further attempts, with the recently developed self-learning determinantal quantum Monte Carlo scheme [53–55], which can greatly reduce the autocorrelation at the (quantum) critical point and speed up the simulation with the $\mathcal{O}(N)$ fold, to access larger L and lower T are in progress.

APPENDIX B: Z-DIRECTION FLUX

To reduce spurious finite-size effects, we have used the techniques introduced in Ref. [56]. The basic idea is to introduce an effective z-direction flux by multiplying the hopping parameter by Peierls phase factors, i.e.,

$$-t\hat{c}_{i\lambda\sigma}^\dagger\hat{c}_{j\lambda\sigma} \to -te^{i\phi_{ij}^{\lambda\sigma}}\hat{c}_{i\lambda\sigma}^\dagger\hat{c}_{j\lambda\sigma},$$

with $\phi_{ij}^{\lambda\sigma} = [(2\pi)/\Phi_0]\int_{\mathbf{r}_i}^{\mathbf{r}_j}\mathbf{A}^{\lambda\sigma}(\mathbf{r})\cdot d\mathbf{r}$.

To make sure the model remains free of the sign problem, we take

$$\phi_{ij}^{1\uparrow} = \phi_{ij}^{1\downarrow} = -\phi_{ij}^{2\uparrow} = -\phi_{ij}^{2\downarrow}; \quad \text{(B1)}$$

therefore, the applied flux is not a true magnetic field, as it couples differently to fermions of different flavors.

Translational invariance imposes restrictions on the magnitude of the effective magnetic field, namely, $B^{\lambda\sigma} = n(\Phi_0/L^2)$, with n an integer and Φ_0 the flux quanta. We use the Landau gauge $\mathbf{A}^{\lambda\sigma}(\mathbf{r}) = -B^{\lambda\sigma}y\hat{\mathbf{x}}$ in the bulk of the system, whereas special care is taken at the "edges",

$$\phi_{i(x,y=L);j(x,y=1)}^{\lambda\sigma} = \frac{2\pi}{\Phi_0}B^{\lambda\sigma}Lx, \quad \text{(B2)}$$

$$\phi_{i(x,y=1);j(x,y=L)}^{\lambda\sigma} = -\frac{2\pi}{\Phi_0}B^{\lambda\sigma}Lx. \quad \text{(B3)}$$

While applying a flux in the z direction dramatically improves the convergence to the thermodynamic limit, it also breaks translation symmetry, making it impossible to extract the momentum dependence of fermionic correlations. Whenever such information is needed [such as for the momentum-resolved, singlet-particle Green's function $G_{\mathbf{k}}(\omega_n)$], we apply a flux in the x or y direction, which is equivalent to twisting the boundary conditions. Just as in the case of the z-directed flux, choosing Eq. (B1) ensures the absence of the sign problem [57]. We have used six kinds of twisted boundary conditions, (0,0), $(\pi/2,0)$, $(\pi/2,\pi/2)$, $(\pi,0)$, $(\pi,\pi/2)$, and (π,π); thus, we get 16 times higher resolution of momentum.

APPENDIX C: THERMAL PHASE TRANSITION

The thermal phase boundary in Fig. 1(b) of the main text is controlled by the 2D Ising critical exponents $\gamma = 7/4$ and $\nu = 1$, implying that the zero-frequency and zero-momentum Ising spin susceptibility around the finite-temperature critical field h_N satisfies

$$\chi(h,T,0,0) = L^{\gamma/\nu}f((h-h_N)L^{1/\nu}). \quad \text{(C1)}$$

Here, the Ising spin susceptibility is defined as

$$\chi(h,T,\mathbf{q},i\omega_n)=\frac{1}{L^2}\sum_{ij}\int_0^\beta d\tau e^{i\omega_n\tau-i\mathbf{q}\cdot\mathbf{r}_{ij}}\langle s_i^z(\tau)s_j^z(0)\rangle. \tag{C2}$$

Figure 6(a) illustrates the behavior of $\chi(h,T,0,0)$ at fixed temperature $T=0.5$ as a function of transverse field; Fig. 6(b) is the data collapse according to Eq. (C1), from which we can obtain $h_N(T=0.5)\approx 3.06$. Because of the coupling between the fermions and the Ising spins, the fermions go through the same finite-temperature phase transition, as shown in Fig. 7(a). The fermionic spin susceptibility $\chi_{\mathrm{F}}(h,T,0,0)$, where

$$\chi_{\mathrm{F}}(h,T,\mathbf{q},\omega_n)=\frac{1}{L^2}\int d\tau\sum_{ij\lambda\lambda'}e^{i\omega_n\tau-i\mathbf{q}\mathbf{r}_{ij}}\langle\sigma_{i\lambda}^z(\tau)\sigma_{j\lambda'}^z(0)\rangle, \tag{C3}$$

behaves much like $\chi(h,T,0,0)$, and a data collapse, shown in Fig. 7(b), gives rise to the same $h_N(T=0.5)\approx 3.06$.

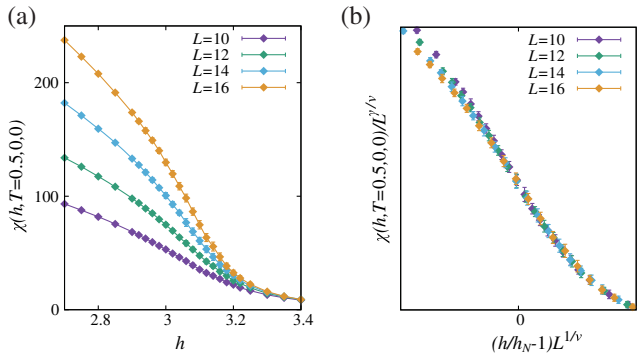

FIG. 6. Finite-temperature FM-to-PM phase transition at $T=0.5$. Panel (a) shows the Ising spin susceptibility at $\mathbf{q}=0$ and $\omega_n=0$, and panel (b) shows the data collapse according to Eq. (C1). Note that h_N is a free fitting parameter, and the best data collapse gives $h_N(T=0.5)\approx 3.06$.

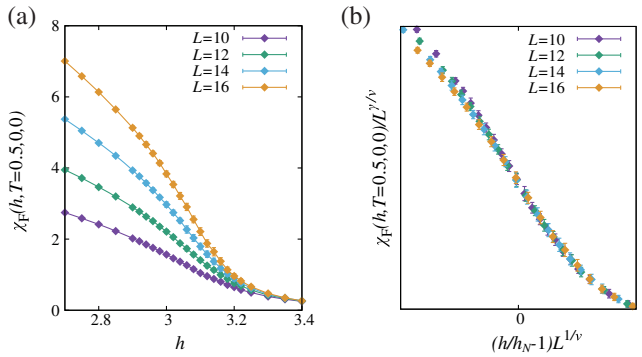

FIG. 7. Finite-temperature FM-to-PM phase transition at $T=0.5$. Panel (a) shows the fermion spin susceptibility at $\mathbf{q}=0$ and $\omega_n=0$, and panel (b) shows the data collapse according to Eq. (C1). Note that h_N is a free fitting parameter and the best data collapse gives $h_N(T=0.5)\approx 3.06$.

APPENDIX D: QUANTUM CRITICAL SCALING ANALYSIS OF $\chi(h,T,0,0)$

In the main text, we have discussed the dynamic Ising spin susceptibility, $\chi(h,T,\mathbf{q},\omega_n)$, and performed the quantum critical scaling analysis. Here, we reveal more details.

According to Eq. (10) in the main text, at $\mathbf{q}=\mathbf{0}$ and $\omega_n=0$, we have

$$\chi(h,T,\mathbf{0},0)=\frac{1}{c_tT^{a_t}+c_h|h-h_c|^{\gamma}}. \tag{D1}$$

We detect the power in T by measuring $\chi(h=h_c,T,\mathbf{0},0)$, and Fig. 8 shows the fitting of $\chi(h=h_c,T,\mathbf{0},0)^{-1}=c_tT^{a_t}$.

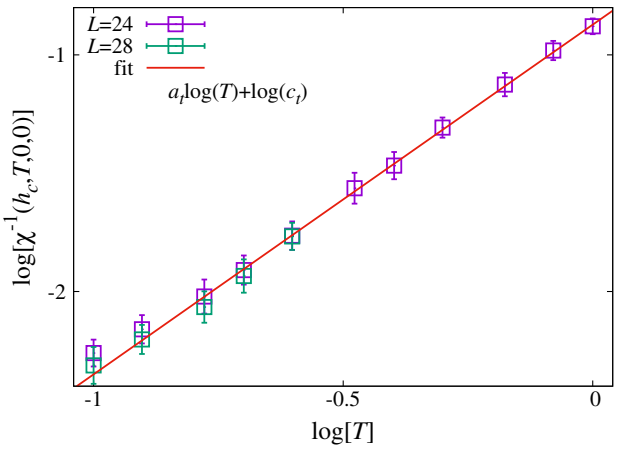

FIG. 8. Inverse Ising spin susceptibility at QCP $[\chi^{-1}(h_c,T,\mathbf{0},0)]$ as a function of temperature T. The slope of the log-log plot reveals the power $a_t=1.48(4)$, and the intercept gives rise to the prefactor $c_t=0.13(1)$.

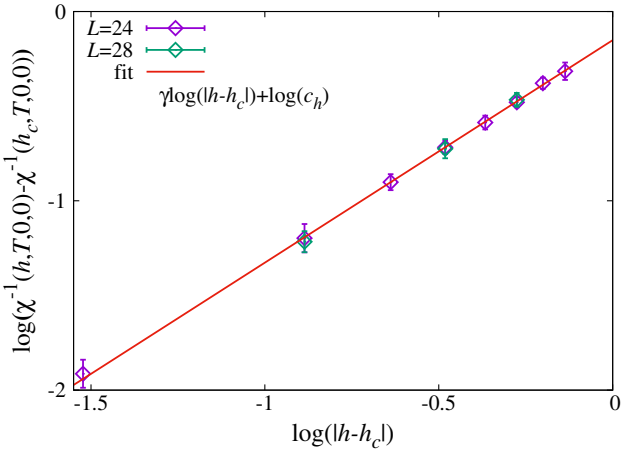

FIG. 9. Inverse Ising spin susceptibility $[\chi(h,T=0.1,\mathbf{0},0)]$ away from QCP $(h>h_c)$ as a function of $|h-h_c|$. Here, the temperature is $T=0.1$, and $\chi^{-1}(h_c,T=0.1,\mathbf{0},0)$ has been deducted in the plot. The slope of the log-log plot reveals the power $\gamma=1.18(4)$, and the intercept gives rise to the prefactor $c_h=0.7(1)$.

The fit gives rise to $c_t = 0.13(1)$ and $a_t = 1.48(4)$. We further detect the power in transverse field h by fitting $\chi(h, T, \mathbf{0}, 0)^{-1} - \chi(h_c, T, \mathbf{0}, 0)^{-1} = c_h|h - h_c|^{\gamma}$, as shown in Fig. 9. The fit gives rise to $c_h = 0.7(1)$ and $\gamma = 1.18(4)$.

APPENDIX E: EFFECTIVE ATTRACTION AND BCS ANALYSIS

In this section, we examine the effective attraction induced by the Ising-field fluctuations. Away from the critical point, the Ising spins are gapped, and we can therefore integrate them out, obtaining an effective four-fermion interaction,

$$S_{\text{int}} = -\frac{\xi^2}{2}\int d\tau d\tau' \sum_{ij\lambda\lambda'} \sigma^z_{i\lambda}(\tau)\chi(h, T, \mathbf{r}_i - \mathbf{r}_j, \tau - \tau')\sigma^z_{j\lambda'}(\tau'). \tag{E1}$$

This interaction contains two types of terms: (a) attractions, e.g., $n_{\lambda\uparrow}n_{\lambda'\uparrow}$, and (b) repulsions, $n_{\lambda\uparrow}n_{\lambda'\downarrow}$. Focusing on instabilities in the particle-particle channel, only attractive interactions will be considered. We are therefore restricted to pairing of fermions of equal spin. Within the BCS approximation, to gain the most free energy, a nodeless order parameter is preferable. Thus, to satisfy the Pauli principle, the order parameter must transform as a singlet under orbital rotations. This implies that the effective attraction favors pairing in the channels $\Delta_{i,\sigma} = c_{i1\sigma}c_{i2\sigma}$ as well as their linear superpositions. These are the pairing channels that are most favored by the ferromagnetic fluctuations. As shown in Sec. VI of the main text, our QMC results show that, indeed, pairing correlations in these channels are enhanced near the FM QCP.

APPENDIX F: POSSIBLE SUPERCONDUCTING PHASES

The two-component nature of the superconducting order parameter Eq. (11) may give rise to a number of exotic phases. Although our numerical data do not show evidence of such phases, in this section we describe how these phases could be detected. We restrict our attention to the paramagnetic phase since the two components, $\Delta_\uparrow$, $\Delta_\downarrow$, are related by the Z_2 symmetry of the model. Define $\Delta_\sigma = \Delta e^{i\theta_\sigma}$, and switch to the charge-spin basis,

$$\begin{aligned}\theta_\uparrow &= \theta_c + \theta_s,\\ \theta_\downarrow &= \theta_c - \theta_s.\end{aligned} \tag{F1}$$

Neglecting amplitude fluctuations, the classical phase action is therefore $S = S_c + S_s$, with

$$S_{c,s} = \frac{1}{2}\int d^2 r K_{c,s}(\nabla\theta_{c,s})^2. \tag{F2}$$

The possible phases (apart from a disordered phase) are as follows:

(1) Charge-4e superconductor: θ_c is quasi-long-range ordered, while θ_s is short ranged. An appropriate order parameter is $\Delta_\uparrow\Delta_\downarrow \propto e^{i2\theta_c}$, whose correlations go as $\langle(\Delta^\dagger_\uparrow\Delta^\dagger_\downarrow)(\mathbf{r})(\Delta_\downarrow\Delta_\uparrow)(0)\rangle \propto r^{-[4/(2\pi K_c)]}$.

(2) Spin-nematic: θ_s is quasi-long-range ordered, while θ_c is short ranged. The order parameter is $\Delta^\dagger_\uparrow\Delta_\downarrow \propto e^{-i2\theta_s}$, whose correlations go as $\langle(\Delta^\dagger_\uparrow\Delta_\downarrow)(\mathbf{r})(\Delta^\dagger_\downarrow\Delta_\uparrow)(0)\rangle \propto r^{-[4/(2\pi K_s)]}$.

(3) Triplet superconductor: Both sectors have quasi-long-range order. Here, $\Delta_\uparrow$ has power-law correlations, $\langle\Delta^\dagger_\uparrow(\mathbf{r})\Delta_\uparrow(0)\rangle \propto r^{-\{[1/(2\pi K_c)]+[1/(2\pi K_s)]\}}$.

The phase diagram of the same model (in different physical contexts) has been studied in Refs. [44–46]. To determine the phase diagram, we consider the criteria for stability against the appearance of a single vortex. In this model, there are three kinds of vortices:

(1) A vortex of one spin species and an antivortex in the other. Across the branch cut, $\theta_c \to \theta_c$, $\theta_s \to \theta_s + 2\pi$.

(2) A vortex of both spin species. Across the branch cut, $\theta_c \to \theta_c + 2\pi$, $\theta_s \to \theta_s$.

(3) A vortex of one of the spin species. Across the branch cut, $\theta_c \to \theta_c + \pi$, $\theta_s \to \theta_s + \pi$.

The phase diagram can be derived from considering the free energy of a single unpaired vortex, given by $F = E - TS$. (As in the usual Berezinski-Kosterlitz-Thouless transition, such an analysis reproduces the phase diagram from a more rigorous renormalization group treatment.) The stability condition is $F > 0$. The energy of a vortex of type 3 is

$$E_3 = \frac{1}{2}(K_c + K_s)\int d^2 r\left(\frac{\pi}{2\pi r}\right)^2 = \frac{\pi}{4}(K_c + K_s)\log\left(\frac{L}{a}\right),$$

where L is the system size and a is some short-range cutoff. Similarly, $E_2 = \pi K_s \log(L/a)$ and $E_1 = \pi K_c \log(L/a)$. The entropy is the same in all cases, $TS = \log(L^2/a^2)$.

The resulting phase diagram is given in Fig. 10.

The stiffnesses K_c and K_s can be extracted from certain current-current correlation functions [58],

$$\begin{aligned}K_c &= \frac{\beta}{4}(\delta\Lambda_{\uparrow\uparrow} + \delta\Lambda_{\downarrow\downarrow} + 2\delta\Lambda_{\uparrow\downarrow}),\\ K_s &= \frac{\beta}{4}(\delta\Lambda_{\uparrow\uparrow} + \delta\Lambda_{\downarrow\downarrow} - 2\delta\Lambda_{\uparrow\downarrow}).\end{aligned} \tag{F3}$$

Here,

$$\delta\Lambda_{\sigma,\sigma'} = \lim_{L\to\infty}\left[\Lambda^{xx}_{\sigma,\sigma'}\left(q_x = \frac{2\pi}{L}, q_y = 0\right) - \Lambda^{xx}_{\sigma,\sigma'}\left(q_x = 0, q_y = \frac{2\pi}{L}\right)\right], \tag{F4}$$

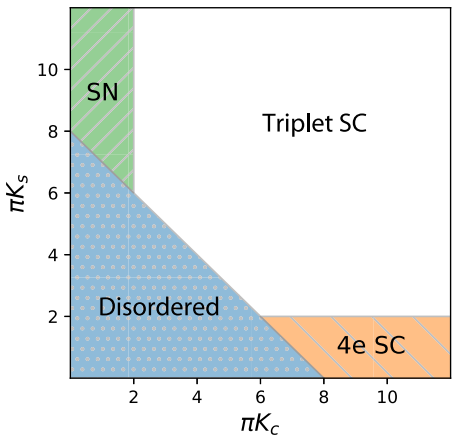

FIG. 10. Phase diagram of the phase action Eq. (F2), illustrating the SN phase, the charge-4e SC phase, and the triplet superconducting phase.

where

$$\Lambda^{xx}_{\sigma,\sigma'}(q_x,q_y)=\frac{1}{L^2}\int d\tau\sum_{ij\lambda\lambda'}e^{i\mathbf{q}(\mathbf{r}_i-\mathbf{r}_j)}\langle j^x_{i\lambda\sigma}(\tau)j^x_{j\lambda'\sigma'}(0)\rangle,$$

and $j^x_{i\lambda\sigma}=ite^{i\phi^{\lambda\sigma}_{i,i+\hat{x}}}c^\dagger_{i\lambda\sigma}c_{i+\hat{x},\lambda\sigma}+\text{H.c.}$ is the current density for fermions of orbital λ and spin σ.

APPENDIX G: SUPERFLUID DENSITY AND PAIRING CORRELATIONS

In this appendix, we provide further details on the numerical evidence for superconductivity.

To identify the leading pairing channel, we considered all possible on-site and nearest-neighbor pairing order parameters and computed the pair structure factor for each channel. In all channels other than the orbital-singlet, spin-triplet channel defined in Eq. (11) of the main text, we find a weak response with no substantial system-size dependence or enhancement close to the FM QCP (not shown).

To test whether there are possible superconductivity instabilities close to the QCP, we measured the superfluid densities ρ_c and ρ_s, which are related to the stiffnesses K_c and K_s defined in Eq. (F3). Here, $\rho_{c,s}=K_{c,s}/\beta$. In Fig. 11, we show the temperature dependence of $\rho_c+\rho_s$. For both sets of parameters, $\rho_c+\rho_s<(8/\pi)T$ at the largest system size, and it decreases with the system size, implying the absence of quasi-long-range superconducting order down to $T=0.025$ (see Fig. 10). Note that upon increasing the coupling strength and decreasing temperature, the finite-size estimates for the superfluid density grow. It is likely that there is a transition to a superconducting phase at higher coupling strengths or lower temperatures.

For completeness, in Figs. 12 and 13, we show ρ_c, ρ_s, respectively.

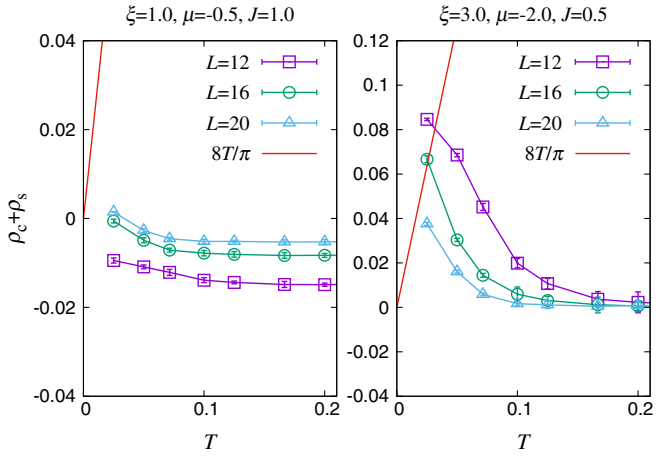

FIG. 11. Temperature dependence of $\rho_c+\rho_s$ at QCP for different system sizes and different couplings.

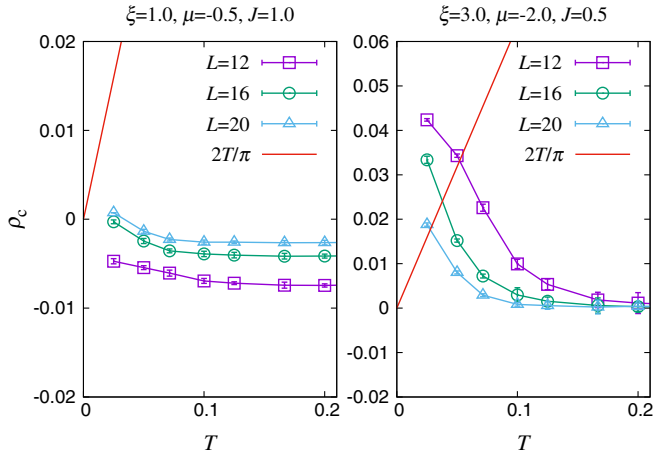

FIG. 12. Temperature dependence of ρ_c at QCP for different system sizes and different couplings.

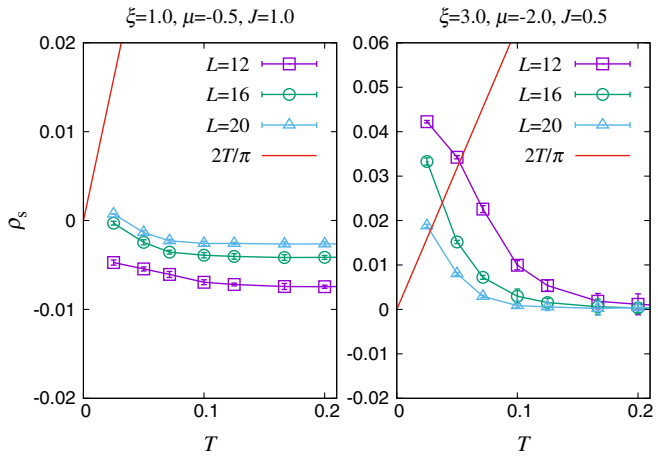

FIG. 13. Temperature dependence of ρ_s at QCP for different system sizes and different couplings.

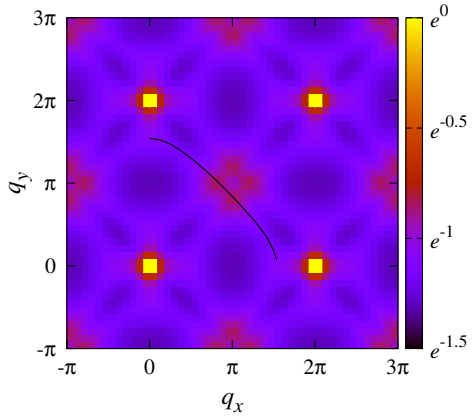

FIG. 14. The intensity distribution of fermion spin susceptibility $\chi_F(h = h_c, T = 0.05, \mathbf{q}, \omega_n = 0)$ with $L = 24$. To amplify the weak signal of the soft mode, we have fixed the intensity range to be less than unity and taken a logarithm of the original data. The black line shows the location of $2\mathbf{k}_F$ for the noninteracting FS, only a quarter of which are plotted here.

APPENDIX H: FERMION SPIN SUSCEPTIBILITY

In Fig. 2(a) of the main text, we discussed the anisotropy of the quasiparticle fraction $Z_{\mathbf{k}_F}(T)$ along the $\theta = 0$ and $\theta = (\pi/4)$ directions, and we associate such anisotropy to the soft fermion-bilinear mode around $\mathbf{Q} = (\pi, \pi)$ in the fermion spin susceptibility, besides the dominant $\mathbf{Q} = (0, 0)$ ferromagnetic fluctuations. Here, we show the fermion spin susceptibility [Eq. (C3)] in Fig. 14 and reveal that it is indeed the case.

Figure 14 shows the fermion spin susceptibility at $h = h_c$, $T = 0.05$ from an $L = 24$ system. The strongest intensity is naturally at $\mathbf{Q} = (0, 0)$; however, near $\mathbf{Q} = (\pi, \pi)$, there are soft modes (the signal is very weak, and we have to fix the intensity range to less than 1 and take a logarithm of the original data).

APPENDIX I: SELF-ENERGY

As shown in Fig. 2 in the main text, the imaginary part of the fermionic self-energy $-\mathrm{Im}\Sigma(\omega_n)$ increases in magnitude as the frequency is lowered. While such behavior is expected in a superconducting state, the superconducting fluctuations were found to be extremely weak. Here, we speculate about the possible mechanism for such behavior.

Close to the classical Ising transition, the dynamics of the order parameter are slow. We focus on the classical fluctuations of the Ising spins, i.e., their static configurations. For each such static configuration, one may solve the fermionic part of the Hamiltonian and obtain the single-particle Green's function. Let us further assume that the fluctuations are extremely sharply peaked at $q = 0$. Then, in a Monte Carlo simulation, the configurations alternate between static, nearly spatially uniform configurations of Ising spins. Most importantly, the sign of the order parameter changes between these configurations, or else the system is, by definition, in the ordered phase. Hence, neglecting all other interaction effects, the fermionic Green's function takes the form

$$G(\mathbf{k}, i\omega_n) \approx \frac{1}{2}\left(\frac{1}{i\omega_n - \epsilon_k - \Delta} + \frac{1}{i\omega_n - \epsilon_k + \Delta}\right), \quad \text{(I1)}$$

where Δ is the magnitude of the local ferromagnetic order parameter. If $\epsilon_k \ll \Delta$, ω, at the nominal Fermi surface ($\epsilon_k = 0$), we find that

$$-\mathrm{Im}\Sigma(i\omega_n) = \mathrm{Im}[G^{-1}(\mathbf{k}, i\omega_n)] - \omega_n = \frac{\Delta^2}{\omega_n},$$

which increases rapidly as the frequency is lowered. If Δ were large, compared, e.g., to temperature, it would be possible to measure it by other means. This would also imply $|\mathrm{Im}\Sigma(i\omega_0)| \gg \omega_0 = \pi T$. Small gaps, however, are difficult to detect.

[1] J. A. Hertz, *Quantum Critical Phenomena*, Phys. Rev. B **14**, 1165 (1976).

[2] A. J. Millis, *Effect of a Nonzero Temperature on Quantum Critical Points in Itinerant Fermion Systems*, Phys. Rev. B **48**, 7183 (1993).

[3] Toru Moriya, *Spin Fluctuations in Itinerant Electron Magnetism* (Springer-Verlag, Berlin, Heidelberg, 1985).

[4] G. R. Stewart, *Non-Fermi Liquid Behavior in d- and f-Electron Metals*, Rev. Mod. Phys. **73**, 797 (2001).

[5] A. V. Chubukov, C. Pépin, and J. Rech, *Instability of the Quantum-Critical Point of Itinerant Ferromagnets*, Phys. Rev. Lett. **92**, 147003 (2004).

[6] H. V. Löhneysen, A. Rosch, M. Vojta, and P. Wölfle, *Fermi-Liquid Instabilities at Magnetic Quantum Phase Transitions*, Rev. Mod. Phys. **79**, 1015 (2007).

[7] A. V. Chubukov and D. L. Maslov, *Spin Conservation and Fermi Liquid Near a Ferromagnetic Quantum Critical Point*, Phys. Rev. Lett. **103**, 216401 (2009).

[8] Y. Li, E. H. Lieb, and C. Wu, *Exact Results for Itinerant Ferromagnetism in Multiorbital Systems on Square and Cubic Lattices*, Phys. Rev. Lett. **112**, 217201 (2014).

[9] S. Xu, Y. Li, and C. Wu, *Sign-Problem-Free Quantum Monte Carlo Study on Thermodynamic Properties and Magnetic Phase Transitions in Orbital-Active Itinerant Ferromagnets*, Phys. Rev. X **5**, 021032 (2015).

[10] J. Custers, P. Gegenwart, H. Wilhelm, K. Neumaier, Y. Tokiwa, O. Trovarelli, C. Geibel, F. Steglich, C. Pepin, and P. Coleman, *The Break-up of Heavy Electrons at a Quantum Critical Point*, Nature (London) **424**, 524 (2003).

[11] A. Steppke, R. Küchler, S. Lausberg, E. Lengyel, L. Steinke, R. Borth, T. Lühmann, C. Krellner, M. Nicklas, C. Geibel, F. Steglich, and M. Brando, *Ferromagnetic Quantum Critical Point in the Heavy-Fermion Metal* $YbNi_4(P_{1-x}As_x)_2$, Science **339**, 933 (2013).

[12] Z. Liu, Y. Gu, W. Zhang, D. Gong, W. Zhang, T. Xie, X. Lu, X. Ma, X. Zhang, R. Zhang *et al.*, *Nematic Quantum Critical Fluctuations in* $BaFe_{2-x}Ni_xAs_2$, Phys. Rev. Lett. **117**, 157002 (2016).

[13] W. Zhang, J. T. Park, X. Lu, Y. Wei, X. Ma, L. Hao, P. Dai, Z. Y. Meng, Y.-f. Yang, H. Luo, and S. Li, *Effect of Nematic Order on the Low-Energy Spin Fluctuations in Detwinned* $BaFe_{1.935}Ni_{0.065}As_2$, Phys. Rev. Lett. **117**, 227003 (2016).

[14] V. Oganesyan, S. A. Kivelson, and E. Fradkin, *Quantum Theory of a Nematic Fermi Fluid*, Phys. Rev. B **64**, 195109 (2001).

[15] W. Metzner, D. Rohe, and S. Andergassen, *Soft Fermi Surfaces and Breakdown of Fermi-Liquid Behavior*, Phys. Rev. Lett. **91**, 066402 (2003).

[16] S.-S. Lee, *Low-Energy Effective Theory of Fermi Surface Coupled with U(1) Gauge Field in* $2+1$ *Dimensions*, Phys. Rev. B **80**, 165102 (2009).

[17] M. A. Metlitski and S. Sachdev, *Quantum Phase Transitions of Metals in Two Spatial Dimensions. I. Ising-Nematic Order*, Phys. Rev. B **82**, 075127 (2010).

[18] M. A. Metlitski and S. Sachdev, *Quantum Phase Transitions of Metals in Two Spatial Dimensions. II. Spin Density Wave Order*, Phys. Rev. B **82**, 075128 (2010).

[19] D. F. Mross, J. McGreevy, H. Liu, and T. Senthil, *Controlled Expansion for Certain Non-Fermi Liquid Metals*, Phys. Rev. B **82**, 045121 (2010).

[20] M. A. Metlitski, D. F. Mross, S. Sachdev, and T. Senthil, *Cooper Pairing in Non-Fermi Liquids*, Phys. Rev. B **91**, 115111 (2015).

[21] T. Holder and W. Metzner, *Anomalous Dynamical Scaling from Nematic and U(1) Gauge Field Fluctuations in Two-Dimensional Metals*, Phys. Rev. B **92**, 041112 (2015).

[22] A. Schlief, P. Lunts, and S.-S. Lee, *Exact Critical Exponents for the Antiferromagnetic Quantum Critical Metal in Two Dimensions*, Phys. Rev. X **7**, 021010 (2017).

[23] D. Dalidovich and S.-S. Lee, *Perturbative Non-Fermi Liquids from Dimensional Regularization*, Phys. Rev. B **88**, 245106 (2013).

[24] S.-S. Lee, *Recent Developments in Non-Fermi Liquid Theory*, arXiv:1703.08172.

[25] A. L. Fitzpatrick, S. Kachru, J. Kaplan, and S. Raghu, *Non-Fermi Liquid Behavior of Large-*N_B *Quantum Critical Metals*, Phys. Rev. B **89**, 165114 (2014).

[26] T. R. Kirkpatrick and D. Belitz, *Nature of the Quantum Phase Transition in Clean Itinerant Heisenberg Ferromagnets*, Phys. Rev. B **67**, 024419 (2003).

[27] D. Belitz, T. R. Kirkpatrick, and T. Vojta, *How Generic Scale Invariance Influences Quantum and Classical Phase Transitions*, Rev. Mod. Phys. **77**, 579 (2005).

[28] S. Lederer, Y. Schattner, E. Berg, and S. A. Kivelson, *Enhancement of Superconductivity Near a Nematic Quantum Critical Point*, Phys. Rev. Lett. **114**, 097001 (2015).

[29] E. Berg, M. A. Metlitski, and S. Sachdev, *Sign-Problem-Free Quantum Monte Carlo of the Onset of Antiferromagnetism in Metals*, Science **338**, 1606 (2012).

[30] Y. Schattner, S. Lederer, S. A. Kivelson, and E. Berg, *Ising Nematic Quantum Critical Point in a Metal: A Monte Carlo Study*, Phys. Rev. X **6**, 031028 (2016).

[31] Y. Schattner, M. H. Gerlach, S. Trebst, and E. Berg, *Competing Orders in a Nearly Antiferromagnetic Metal*, Phys. Rev. Lett. **117**, 097002 (2016).

[32] Z.-X. Li, F. Wang, H. Yao, and D.-H. Lee, *The Nature of Effective Interaction in Cuprate Superconductors: A Sign-Problem-Free Quantum Monte-Carlo Study*, Phys. Rev. B **95**, 214505 (2017).

[33] Z.-X. Li, F. Wang, H. Yao, and D.-H. Lee, *What Makes the* T_c *of Monolayer FeSe on* $SrTiO_3$ *So High: A Sign-Problem-Free Quantum Monte Carlo Study*, Science bulletin **61**, 925 (2016).

[34] X. Y. Xu, K. S. D. Beach, K. Sun, F. F. Assaad, and Z. Y. Meng, *Topological Phase Transitions with SO(4) Symmetry in* $(2+1)$D *Interacting Dirac Fermions*, Phys. Rev. B **95**, 085110 (2017).

[35] S. Lederer, Y. Schattner, E. Berg, and S. A. Kivelson, *Superconductivity and Non-Fermi Liquid Behavior Near a Nematic Quantum Critical Point*, Proc. Natl. Acad. Sci. U.S.A. **114**, 4905 (2017).

[36] F. F. Assaad and T. Grover, *Simple Fermionic Model of Deconfined Phases and Phase Transitions*, Phys. Rev. X **6**, 041049 (2016).

[37] S. Gazit, M. Randeria, and A. Vishwanath, *Emergent Dirac Fermions and Broken Symmetries in Confined and Deconfined Phases of* Z_2 *Gauge Theories*, Nat. Phys. **13**, 484, advance online publication (2017).

[38] P. Pfeuty and R. J. Elliott, *The Ising Model with a Transverse Field. II. Ground State Properties*, J. Phys. C **4**, 2370 (1971).

[39] C. Wu and S.-C. Zhang, *Sufficient Condition for Absence of the Sign Problem in the Fermionic Quantum Monte Carlo Algorithm*, Phys. Rev. B **71**, 155115 (2005).

[40] G. G. Batrouni and R. T. Scalettar, *Quantum Phase Transitions*, in *Ultracold Gases and Quantum Information* Lecture Notes of the Les Houches Summer School in Singapore (Oxford University Press, Oxford, 2011), Vol. 91.

[41] N. Trivedi and M. Randeria, *Deviations from Fermi-Liquid Behavior Above* T_c *in 2D Short Coherence Length Superconductors*, Phys. Rev. Lett. **75**, 312 (1995).

[42] T. Senthil, *Critical Fermi Surfaces and Non-Fermi Liquid Metals*, Phys. Rev. B **78**, 035103 (2008).

[43] K.-S. Chen, Z. Y. Meng, T. Pruschke, J. Moreno, and M. Jarrell, *Lifshitz Transition in the Two-Dimensional Hubbard Model*, Phys. Rev. B **86**, 165136 (2012).

[44] F. Krüger and S. Scheidl, *Nonuniversal Ordering of Spin and Charge in Stripe Phases*, Phys. Rev. Lett. **89**, 095701 (2002).

[45] D. Podolsky, S. Chandrasekharan, and A. Vishwanath, *Phase Transitions of* $s=1$ *Spinor Condensates in an Optical Lattice*, Phys. Rev. B **80**, 214513 (2009).

[46] E. Berg, E. Fradkin, and S. A. Kivelson, *Charge-4e Superconductivity from Pair-Density-Wave Order in Certain High-Temperature Superconductors*, Nat. Phys. **5**, 830 (2009).

[47] Y.-F. Jiang, Z.-X. Li, S. A. Kivelson, and H. Yao, *Charge-4e Superconductors: A Majorana Quantum Monte Carlo Study*, Phys. Rev. B **95**, 241103 (2017).

[48] E. Morosan, H. W. Zandbergen, Lu Li, M. Lee, J. G. Checkelsky, M. Heinrich, T. Siegrist, N. P. Ong, and

R. J. Cava, *Sharp Switching of the Magnetization in* $Fe_{1/4}TaS_2$, Phys. Rev. B **75**, 104401 (2007).
[49] Y. Q. Liu, S. J. Zhang, J. L. Lv, S. K. Su, T. Dong, G. Chen, and N. L. Wang, *Revealing a Triangular Lattice Ising Antiferromagnet in a Single-Crystal* $CeCd_3As_3$, arXiv: 1612.03720.
[50] www.gauss-centre.eu
[51] www.lrz.de
[52] U. Wolff, *Collective Monte Carlo Updating for Spin Systems*, Phys. Rev. Lett. **62**, 361 (1989).
[53] J. Liu, Y. Qi, Z. Y. Meng, and L. Fu, *Self-Learning Monte Carlo Method*, Phys. Rev. B **95**, 041101 (2017).
[54] J. Liu, H. Shen, Y. Qi, Z. Y. Meng, and L. Fu, *Self-Learning Monte Carlo in Fermion Systems*, Phys. Rev. B **95**, 241104 (2017).
[55] X. Y. Xu, Y. Qi, J. Liu, L. Fu, and Z. Y. Meng, *Self-Learning Determinantal Quantum Monte Carlo Method*, Phys. Rev. B **96**, 041119 (2017).
[56] F. F. Assaad and H. G. Evertz, *World-Line and Determinantal Quantum Monte Carlo Methods for Spins, Phonons and Electrons*, in *Computational Many-Particle Physics, Lecture Notes in Physics*, Vol. 739, edited by H. Fehske, R. Schneider, and A. Weiße (Springer, Berlin, Heidelberg, 2008), pp. 277–356.
[57] M. H. Gerlach, Y. Schattner, E. Berg, and S. Trebst, *Quantum Critical Properties of a Metallic Spin-Density-Wave Transition*, Phys. Rev. B **95**, 035124 (2017).
[58] D. J. Scalapino, S. R. White, and S. Zhang, *Insulator, Metal, or Superconductor: The Criteria*, Phys. Rev. B **47**, 7995 (1993).